RSC Advances

PAPER

Cite this: *RSC Adv.*, 2025, **15**, 2347

Construction of a Bi-doped g-C_3N_4/Bi_2MoO_6 ternary nanocomposite for the effective photodegradation of ofloxacin under visible light irradiation†

Priti Rohilla,[a] Bonamali Pal*[ab] and Raj Kumar Das *[ab]

Water contamination is a result of the excessive use of antibiotics nowadays. Owing to this environmental toxicity, photocatalytic degradation is the primary approach to non-biological degradation for their removal. In this context, zerovalent Bi-doped g-C_3N_4/Bi_2MoO_6 [g-C_3N_4/Bi@Bi_2MoO_6] ternary nanocomposite was prepared using the wet impregnation method. Surprisingly, zerovalent Bi is generated simultaneously during the hydrothermal synthesis of Bi_2MoO_6 without using any additional reducing agent. The performance of the synthesized catalyst for the removal of ofloxacin is measured using visible light radiation. Various techniques like XRD, XPS, DRS, HRTEM, FESEM, *etc.*, were used to characterize the nanocomposites. Additionally, XPS, DRS, and HRTEM confirm the presence of zerovalent Bi. The degradation efficiency was recorded as 82% after 3 h for the optimized catalyst. The control experiments confirm that the superoxide radicals and holes function as reactive entities in the degradation process. HRMS was used to identify the intermediates and various fragments, which support the suggested mechanism. The photocatalyst exhibits outstanding stability and reusability. Due to its stability, easy synthesis, excellent catalytic activity, and reusability, the reported photocatalyst can be considered to be an excellent candidate for photocatalytic pollutant degradation.

Received 2nd December 2024
Accepted 17th January 2025

DOI: 10.1039/d4ra08493d

rsc.li/rsc-advances

1. Introduction

The discharge of effluent containing organic pollutants and toxins into the environment has significant risks for the biosphere and is a serious health threat to humans.[1] Among these pollutants are antibiotics, commonly used to treat bacterial infections.[2]

Among the antibiotics, ofloxacin is a frequently used fluoroquinolone-based drug found in surface water at up to 31.7 μg L^{-1} concentrations. Even at very low concentrations, ofloxacin can have a detrimental effect on ecological systems by preventing the growth of microorganisms and producing other ecotoxicological effects.[3–7] Hence, it is crucial to remove these pollutants from wastewater.[8,9] Many methods have been developed so far, including nano-filtration, coagulation, ion exchange, photocatalysis, adsorption, *etc.* One of the most appealing methods for treating wastewater is photocatalysis as it causes the contaminants to entirely break down rather than merely shifting from one medium to another.[10] In recent years, semiconductor catalysed photocatalytic degradation of organic contaminants has grown significantly by consuming solar light energy due to increasing environmental concerns.[11–14]

Bi_2MoO_6, an Aurivillius oxide, exhibits interesting physicochemical properties, such as a band gap of nearly 2.7 eV. This unique semiconductor reveals excellent performance under visible light irradiation. Its structure includes $[MoO_4]^{-2}$ alternate sheets with $[Bi_2O_2]^{+2}$ layers, distinguishing it from other bismuth-based materials.[15] However, because of the low separation efficiency of the photoexcited charge carriers, Bi_2MoO_6 is insufficiently efficient to meet the requirements of the application.[16] This drawback can be avoided by using various approaches like porosity engineering, elemental doping, semiconductor modification by creating heterojunction structures, *etc.*[17] Because of its high stability and low cost, g-C_3N_4 is a promising material for making semiconductor heterojunctions. Other advantages include strong physicochemical stability, a 2.7 eV band gap, non-toxicity, and a large surface area.[10]

Furthermore, photocatalytic activity is increased by loading various plasmonic metals due to their localised surface plasmon resonance (LSPR) properties, which help to separate charge carriers and excite electron–hole pairs.[18] Bismuth (Bi), a non-noble metal, exhibits a significant LSPR effect along with

---

[a] *Department of Chemistry and Biochemistry, Thapar Institute of Engineering & Technology, Patiala 147004, Punjab, India. E-mail: bpal@thapar.edu; rkdas@thapar.edu*

[b] *TIET-Virginia Tech Center of Excellence in Emerging Materials, Thapar Institute of Engineering & Technology, Patiala 147004, Punjab, India*

† Electronic supplementary information (ESI) available. See DOI: https://doi.org/10.1039/d4ra08493d

plasmonic metals (Cu, Ag, Au). One benefit of bismuth over noble metals is its affordable price. This study includes the fabrication of a Bi-doped g-C_3N_4/Bi_2MoO_6 ternary composite and examines its photoactivity for the degradation of ofloxacin. To fabricate Bi-doped Bi_2MoO_6, a hydrothermal method was adopted in which methanol was used as a solvent. Remarkably, Bi(+3) does not need any extra step for the reduction process as methanol itself works as a reducing agent here, reducing Bi(+3) *in situ* during hydrothermal reaction. The wet impregnation method was used for the successful loading of g-C_3N_4. The presence of Bi(0) and g-C_3N_4 can increase the light sensitivity and decrease the charge carriers (e^- and h^+) recombination. Such characteristics can be beneficial to enhance the photocatalytic activity.

2. Experimental

2.1 Chemicals

Chemical reagents: $[Bi(NO_3)_3\cdot 5H_2O]$ 98%, sodium molybdate dihydrate 99% $[Na_2MoO_4\cdot 2H_2O]$, urea extra pure 99%, methanol 99.5% extra pure and *N*-methyl-2-pyrrolidone (NMP) were obtained from Loba Chemie, India. Changshu Hongsheng Fine Chemicals Co. Ltd has provided the absolute 99.9% ethanol. Antibiotic ofloxacin (200 mg) was purchased from Cipla Pharmaceutical, and DI (distilled water) was produced using the Milli-Q Millipore system. The fluorinated tin oxide (FTO) coated glasses were bought from Vritra Technologies (resistance < 10 Ω). Carbon black powder (CB) and polyvinylidene fluoride (PVDF) were purchased from Nanoshell and Sigma Aldrich, respectively.

2.2 Preparation of Bi@Bi_2MoO_6

Solvothermal method was used to synthesis Bi@Bi_2MoO_6, 0.25 M of $Na_2MoO_4\cdot 2H_2O$ and bismuth nitrate pentahydrate (0.5 M) were mixed in 35 mL of distilled water and 35 mL of methanol respectively and stirred for 2 h. The above mixture was kept in an autoclave of 100 mL at 180 °C for 24 h,[19] then centrifuged and dried at 70 °C and will be denoted as BM in this manuscript.

2.3 Synthesis of g-C_3N_4

To synthesis g-C_3N_4 sheets using urea as a raw material was prepared by pyrolysis followed by the ultrasonication method. 30 g urea in a crucible was heated at 5 °C min^{-1} at 500 °C for 2 h then again to 550 °C at 10 °C min^{-1} for another 2 h. After cooling down naturally, the pale yellow-coloured powder was ground into bulk g-C_3N_4. The obtained product was dispersed in ethanol for 1 h using ultrasonication to attain g-C_3N_4 sheets, then the solution was filtered and dried at 50 °C. It will be abbreviated as g-CN in the entire manuscript.[20]

2.4 Synthesis of g-CN loaded BM nanocomposite

The g-C_3N_4/Bi@Bi_2MoO_6 composite was prepared *via* the wet impregnation method.[21] For the preparation, 100 mg of Bi_2MoO_6 was mixed with the desired quantity of g-C_3N_4 in 1 : 1 (ethanol and DI water). The solution was kept at stirring for 24 h. Then the product was centrifugated and dehydrated at 50 ° C.[20] Throughout the manuscript, the 5 and 10 wt% g-C_3N_4 loaded Bi@Bi_2MoO_6 composite will be represented as 5GBM and 10GBM respectively.

2.5 Preparation of thin films

The drop-casting method was used to prepare the working electrode for EIS measurement (Nyquist plot). 1 mg PVDF and 50 μL NMP were ground together to form a homogenous paste. Then 1–2 mg carbon black (CB) was added and mixed for an extra 15 min. After that, active material (8 mg) was added to attain a slurry, then it was drop-casted and spread onto the FTO-layered glass and dehydrated for 12 h at 60 °C.

2.6 Photocatalytic activity evaluation

The photocatalytic activity of the synthesised BM and its composite 5GBM and 10GBM were examined using the hazardous pollutant ofloxacin. In a model experiment, an optimized amount (5 mg) of the as-prepared composite was added to a test tube containing 5 mL of ofloxacin solution at a concentration of 20 ppm. To acquire the adsorption–desorption equilibrium, the mixture was stirred for half an hour in the absence of light. Then, for predefined periods, the reaction mixture was exposed to visible light (Wipro Garnet B22-50 W LED having a wavelength of more than 360 nm and light intensity of 5000 lumens). By centrifugation, the catalyst was extracted, and then the concentration of the pollutant was scrutinized using a UV-Vis spectrophotometer. The percentage degradation efficiency was evaluated using the eqn (1):

$$\text{Degradation efficiency}(\%) = \frac{C_0 - C_t}{C_0} \times 100\% \qquad (1)$$

where C_0 is the initial concentration and C_t is the concentration at time "t".

2.7 Characterization technique

To record the crystallographic properties, X-ray diffraction (XRD) was examined by employing a diffractometer of Xpert pro-Cu-Kα (1.54 Å) at 45 kV having a diffraction angle (2θ, 10°–75°). The structural morphology was studied using high-resolution transmission electron microscopy (HRTEM) (JEOL JEM 2100 plus) and field-emission scanning electron microscopy (FESEM) (500 FEG-SEM, Carl-Zeiss Sigma). The energy dispersive spectroscopy (EDS) was examined using BRUKER. JASCO V-750 spectrophotometer was used to measure the DRS (diffused reflectance spectroscopic) of the synthesized samples. The oxidation state was determined using (XPS, Omicron ESCA, Oxford Instrument Germany). The Microtrac Belsorp Mini-II (Bel, Japan, Inc.) was utilized to govern the surface area. The FTIR Spectra were obtained by IR Tracer-100 (Shimadzu). The fragments were studied by high-resolution mass spectrometry (HRMS) using a Waters mass spectrometer (QTOF) with UPLC (XEVO G2 XS) and Ion source Combined APCI and both positive and negative ESI mode to identify the fragments. EIS tests were conducted in the dark using a Biologic (potentiostat, VSP300 at 10 mV, with a 0.1 Hz to 1 MHz frequency range). The threeelectrode system comprised a Pt counter electrode, a BM/10GBM-loaded FTO working electrode, and a standard Ag/AgCl reference electrode in 0.5 M Na_2SO_4 solution. Chemical oxygen demand was measured using Hach COD digestor DRB200, open reflux method followed by APHA 4200 (21 edition).

3. Results and discussion

3.1 XRD studies

The diffraction studies were recorded to analyse the crystallinity and phase purity of the material (Fig. 1). The pattern of g-CN closely matches with the ICDD no. 87-1526 (Fig. 1a).[10] A strong peak at 27.5° corresponds to (002) and another peak at 12.7° (100). The minor peak shift of (002) corresponds to the change in interplanar distance between the graphitic nitride sheets.[22] Moreover, two extra peaks between the range 15° and 25° are due to the layered structure of g-CN. The peaks at 10.8°, 23.4°, 28.2°, 32.5°, 36.0°, 39.5°, 47.1°, 55.4°, 56.3°, 58.4° and 68.2° associated with (020), (111), (131), (002), (151), (042), (212), (331), (133), (262) and (004) planes respectively, which justified with the ICDD no. 72-1524 (Fig. 1b) of the orthorhombic crystal phase of Bi_2MoO_6.[19] Additionally, peaks with respect to (101), (110), and (024) planes are observed at 23.4°, 39.5°, and 55.4°, respectively, corresponding to the structure of Bi_2MoO_6 indicating the presence of Bi metal at Bi_2MoO_6, confirmed with the ICDD no. 44-1246.[16] Moreover, the XRD of synthesized composites 5GBM and 10GBM (Fig. 1c) is almost similar to the bare BM, implying that by introducing g-CN, the structural integrity of the BM is not disrupted. Because of the small amount of loading and lower X-ray scattering coefficient of g-CN than pristine BM, there is no g-CN peaks in the composite.[10,21]

3.2 XPS studies

The chemical composition of the 10GBM composite has been determined using XPS analysis as shown in Fig. 2. The 4f signals of Bi in Bi_2MoO_6 (Fig. 2b) at 158.5 eV (Bi $4f_{7/2}$) and 163.8 eV (Bi $4f_{5/2}$) is attributed to trivalent bismuth [Bi(III)]. Additionally, two other peaks at 156.4 eV and 161.7 eV are referred to as zerovalent Bi which validates that methanol reduces Bi(+3) to zerovalent Bi.[10] Mo(+5) 3d (Fig. 2c) deconvolutes into two peaks, at 231.7 eV and 234.9 eV relative to Mo $3d_{5/2}$ and Mo $3d_{3/2}$, respectively.[23,24] Typically for O 1s (Fig. 2d), lattice oxygen in the crystal structure is assigned to 529.7 eV and 530.3 eV attributed to oxygen vacancies.[25] The XPS spectra of C1s showed four peaks that corresponded to binding energies of 283.9 eV, 286.1 eV, 287.6 eV, and 292.9 eV (Fig. 2e) due to extraneous carbon in the surface, N–C=N bonds, sp^2 hybridised carbon of $(N)_2$–C=N heterocyclic ring and C–NH_2 respectively.[10,26,27] The signals observed at 397.8 eV and 398.7 eV attributed to sp^2 nitrogen of

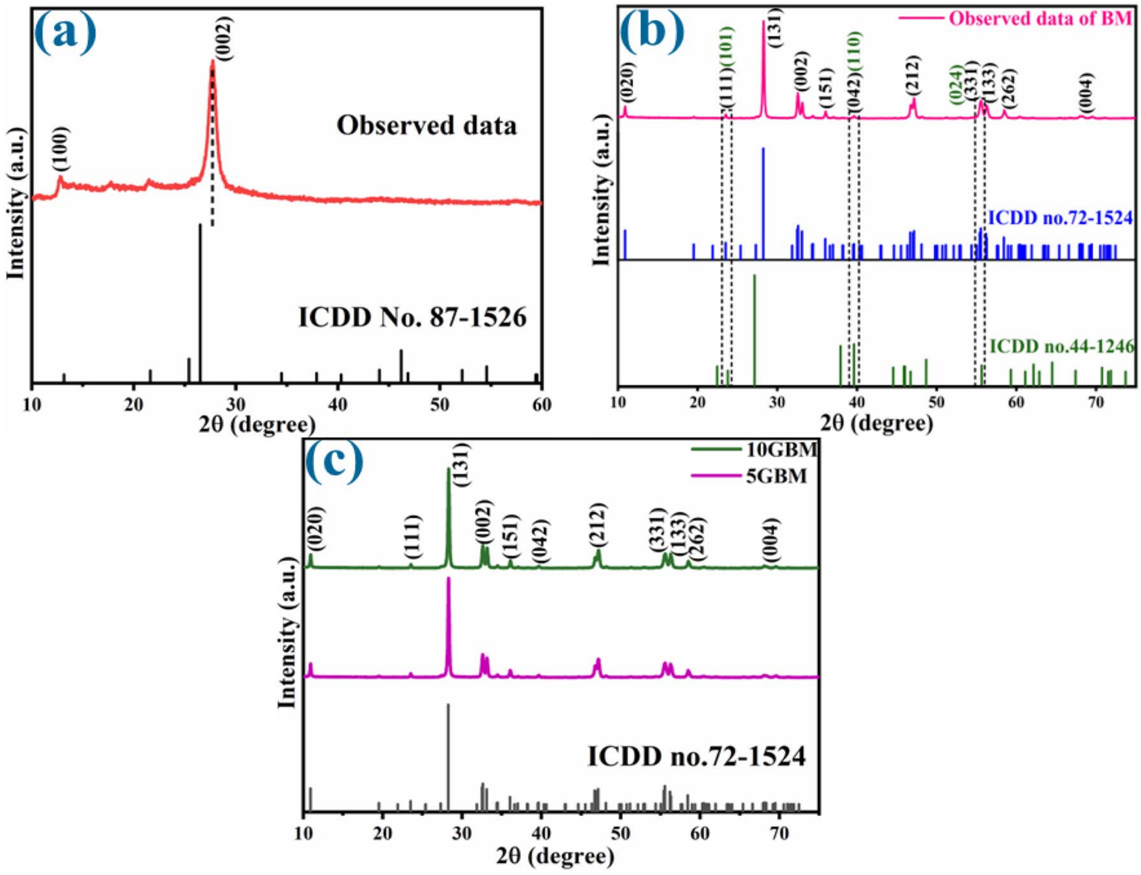

Fig. 1 Diffraction pattern for (a) g-CN (b) pure BM, and (c) as synthesised composites 5GBM and 10GBM.

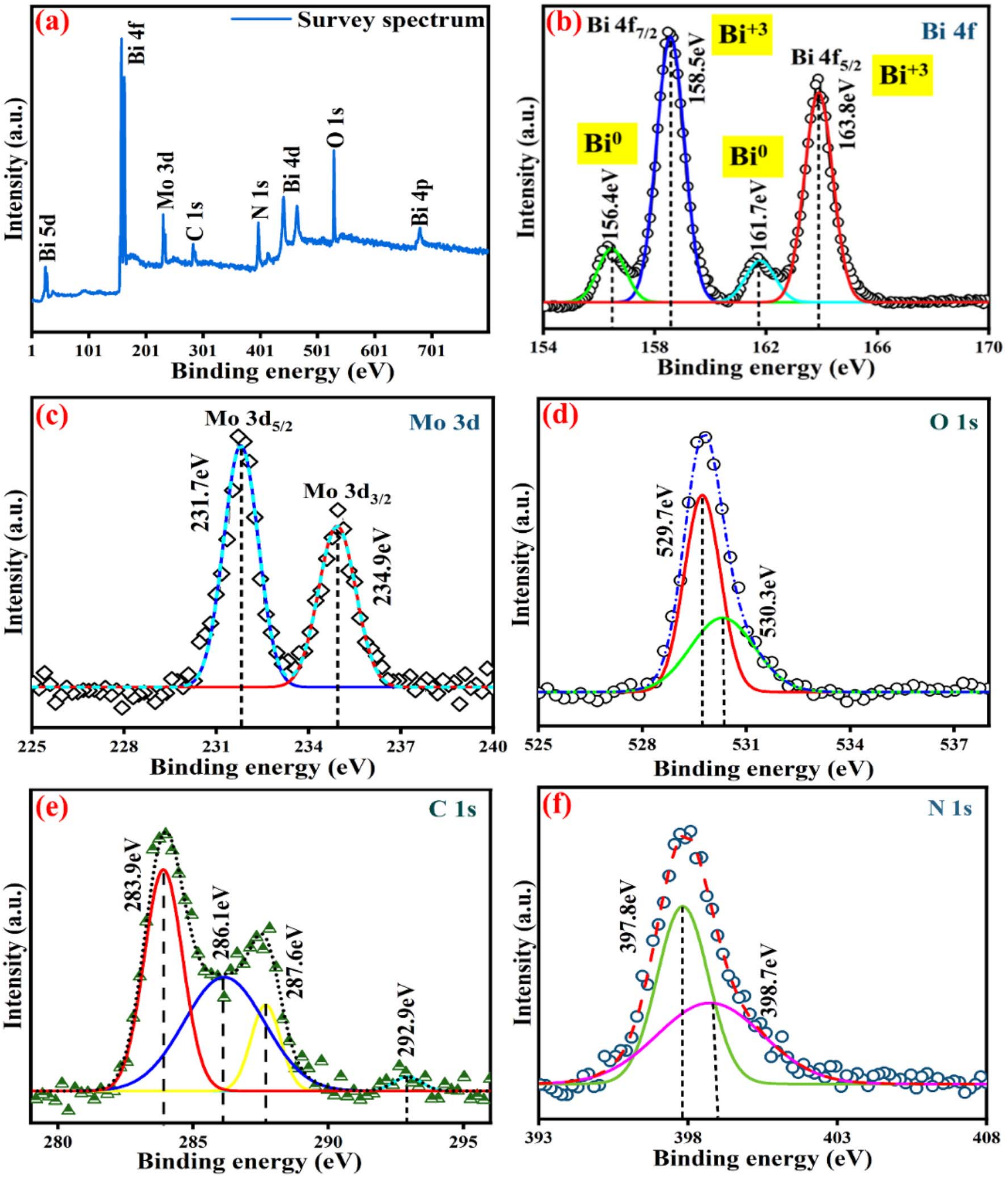

Fig. 2 XPS graphs representing (a) survey diagram (b) Bi [4f] (c) Mo [3d] (d) O [1s] (e) C [1s] and (f) N [1s] of the 10GBM nanocomposite.

triazine rings corresponding to C–N═C and bridged nitrogen atom N–(C)$_3$ respectively (Fig. 2f).[28]

3.3 Optical studies

Optical studies were examined to determine the bandgap of BM and the synthesised nanocomposites. The Bi_2MoO_6 and g-CN have an absorption edge value (Fig. 3a) of 490 nm and 470 nm respectively.[29,30] A broad absorption band at 500–800 nm in the UV-Vis DRS spectra of BM is referred to as the LSPR effect shown by Bi(0).[31] Tauc plot (Fig. 3b and c) indicates that the band gap of BM is 2.55 eV, significantly less than the reported value.[19] This is probably because plasmonic Bi is present in the Bi_2MoO_6 lattice. As g-CN loading increases, the composites' bandgap reduces to 2.40 eV from 2.55 eV, revealing improved absorption of visible light. In contrast, the band gap values at the absorption edge remain practically similar for BM, 5GBM, and 10GBM as shown in Fig. 3c. Such observation is quite similar to the result reported previously[12] and reveals that the loading of g-CN over BM enhances the light sensitivity of the prepared composites.

The PL (photoluminescence) experiments' results are indeterminate because the bare BM showed non-fluorescent behaviour.

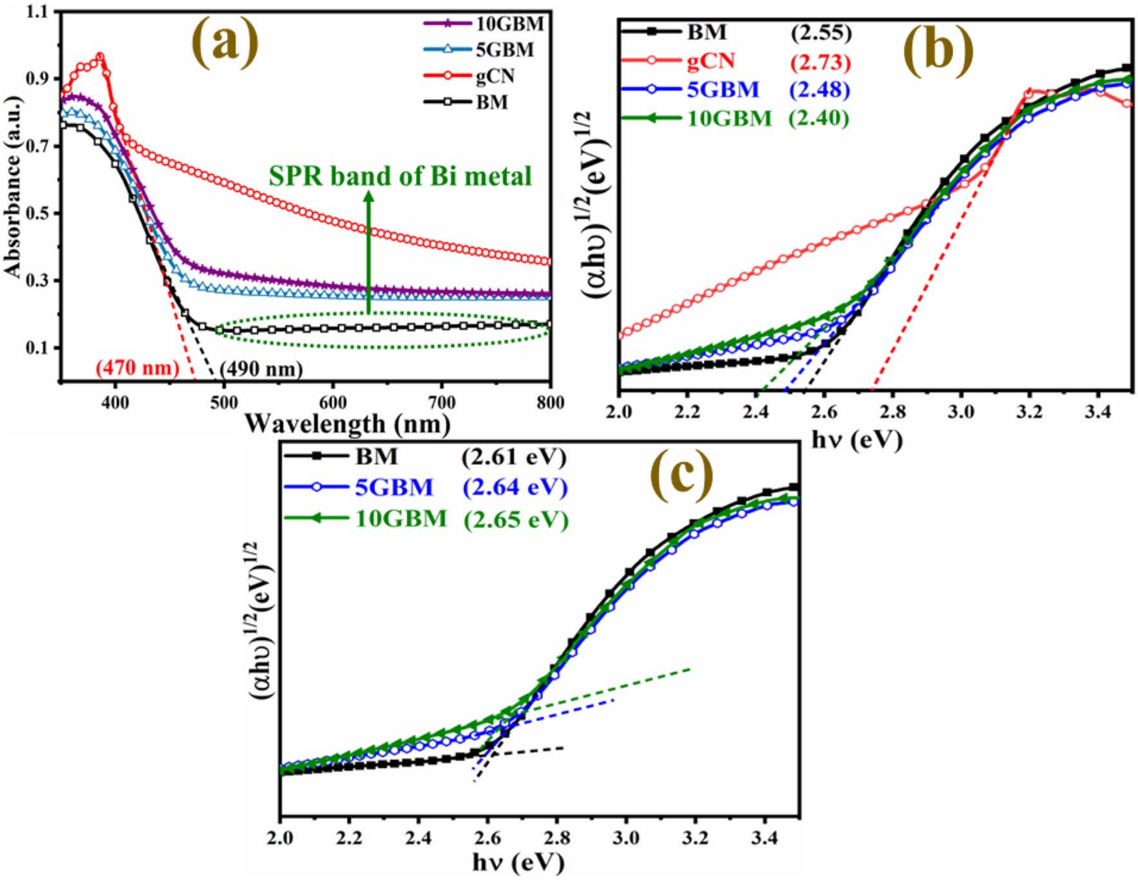

Fig. 3 (a) DRS of BM, g-CN, and all synthesised nanocomposites (b) band gap values and (c) band gap values at absorption edge using Tauc plot.

3.4 FTIR analysis

The synthesised materials were further verified by FTIR analysis. All the nanocomposites 5GBM and 10GBM show peaks of both the bare BM and g-CN (Fig. 4). Several peaks in the region 1100–1700 cm^{-1} are attributed to the C–N heterocycle. The broad band between 3000 and 3400 cm^{-1} is due to the N–H and O–H groups of g-CN. At 810 cm^{-1}, the out-of-plane bending mode of the heptazine unit was detected.

The bands between 400 and 900 cm^{-1} are because of the stretching mode of Bi–O, Mo–O, and the bridging mode of Mo–O–Mo. At 790 cm^{-1}, MoO$_6$ octahedron asymmetric mode was observed.[32]

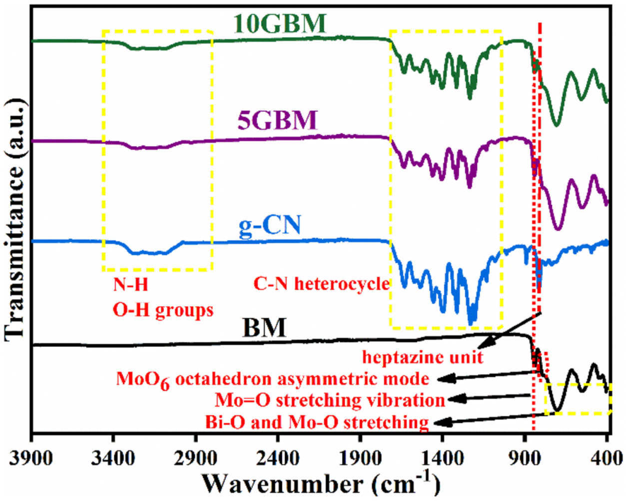

Fig. 4 The FTIR spectra of pristine BM, g-CN and all composites.

3.5 EIS analysis

The EIS analysis was carried out to understand the transfer efficiency of photogenerated charge carriers.[33] The experiment was conducted in the dark for g-CN as well as bare BM and 10GBM composite (Fig. 5). The g-CN has an extremely small charge transfer resistance due to its high conductivity. As a result, the charge transfer resistance[34] of 10GBM composites becomes smaller compared to bare BM as the composite possesses smaller radii in the Nyquist plot compared to its pristine analog, as represented in Fig. 5(b).[35] This indicates that incorporating g-CN helps the electron migration from BM to the g-CN surface. Hence, the composites can serve as more proficient photocatalysts than pristine BM.

3.6 Morphology

The morphology of bare BM and its 10GBM ternary composite were studied using FESEM shown in Fig. 6. Remarkably, the

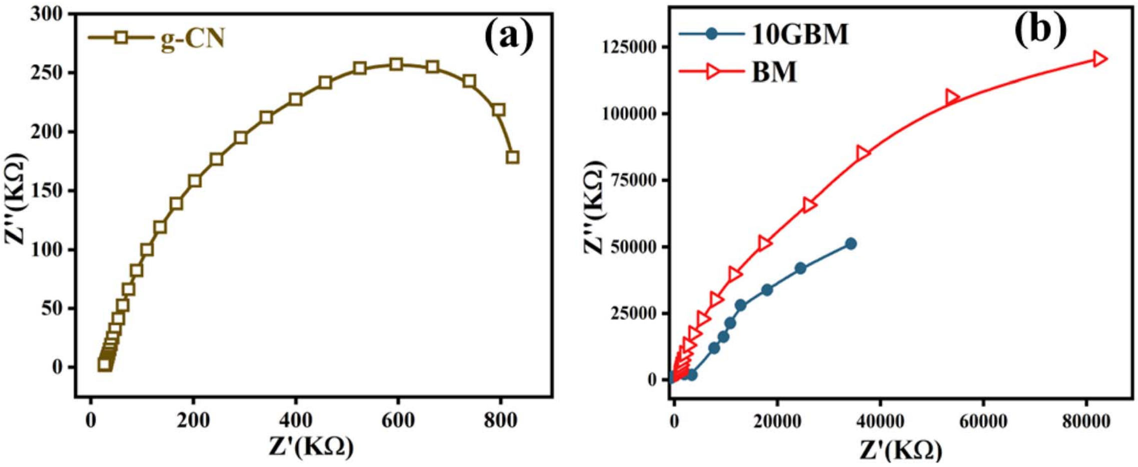

Fig. 5 Nyquist plots of (a) g-CN and (b) bare BM and 10GBM composite.

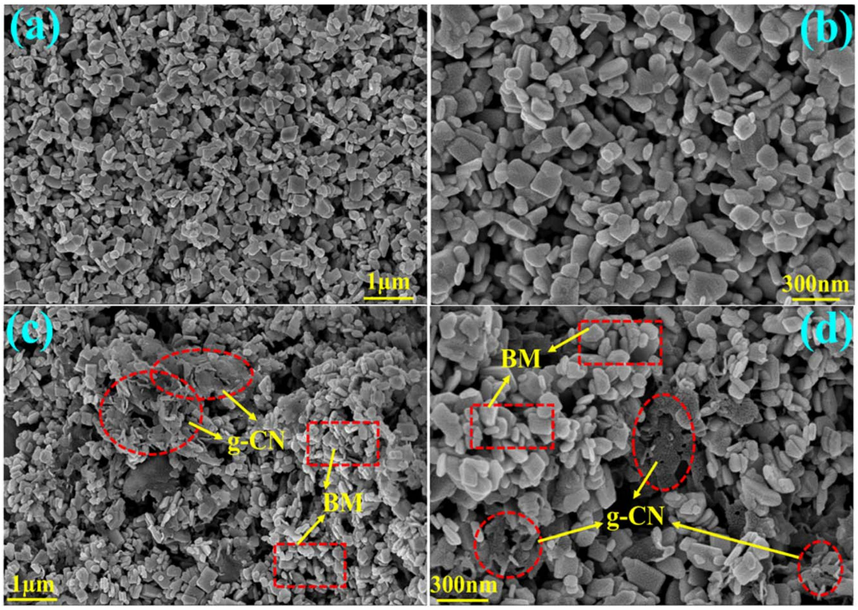

Fig. 6 FESEM images of pristine BM (a and b) and 10GBM nanocomposite (c and d).

pristine Bi_2MoO_6 depicts an irregular crystals-like structure (Fig. 6a and b).[36] The presence of both the CN layers and Bi_2MoO_6 irregular crystals is shown in Fig. 6c and d confirming the development of 10GBM nanocomposite. The elemental mapping (EDS) of the bare BM and nanocomposite 10GBM exhibits every component (Mo, O, Bi, C, and N) elements were uniformly dispersed across the entire surface (Fig. S2 and S3†).

HRTEM analysis (Fig. 7) was conducted to further examine morphology and crystallinity. The heterostructure consists of g-CN, a sheet-like structure of g-CN, and irregular, disorganized particles of Bi_2MoO_6 (Fig. 7a).[37] In Fig. 7b, the loading of g-CN over Bi_2MoO_6 is confirmed. The lighter sheet-like structure corresponds to g-CN while the darker square shape is of BM. Moreover, spherical Bi(0) particle deposition on the BMO surface was also detected in Fig. 7c and d. Additionally, the fringes of BMO and Bi-metal (Fig. 7e and f) were also represented which are well matched with the (151) and (101) planes, respectively. The selected area diffraction pattern in Fig. 7g exhibits the spots that are respective to (002), (131) and (202), (024) planes of BMO and Bi-metal, respectively. The observations validate the crystallinity and formation of 10GBM ternary composite.

The hydrodynamic particle size of the synthesised catalyst is measured using the DLS technique. The particle size of bare BM and g-CN was observed to be 1099 and 771 nm respectively. As the loading of g-CN increases, the size decreases to 411 nm and 338 nm for 5GBM and 10GBM respectively (Fig. S4†) which is due to more hydrophobicity around the catalyst which reduces the hydrodynamic particle size.

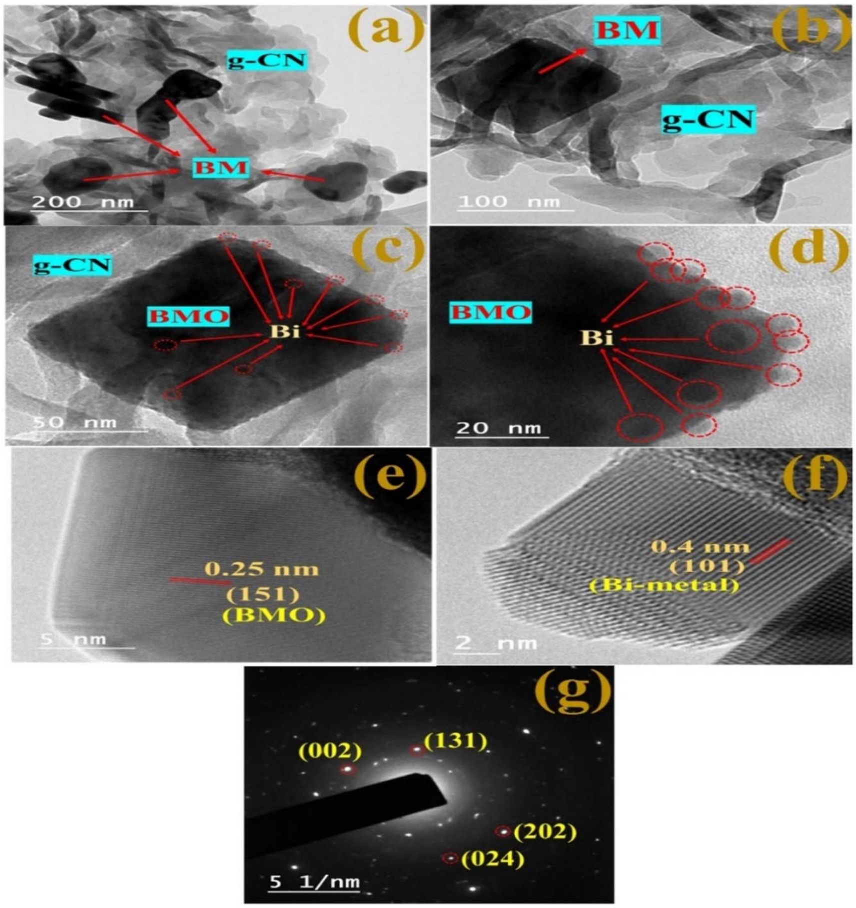

Fig. 7 (a and b) HRTEM micrograph of g-CN and BM, (c and d) showing Bi-metal over BMO and (e and f) lattice fringes (g) selected area diffraction pattern of the synthesised 10GBM ternary nanocomposite.

3.7 N_2 sorption analysis

BET sorption isotherms in Fig. 8 were determined for pristine BM and the 10GBM heterostructure to explain the difference in surface properties after g-CN loading. The prepared samples exhibit an H3 hysteresis loop and type-III sorption isotherm.[38] This indicates the weak adsorbate–adsorbent interaction and implies the occurrence of small pores. Among the two, the 10GBM composite possesses almost double the surface area compared to bare BM due to the incorporation of g-CN which augments the total active sites and resultantly increases the surface area. The total pore volume of bare BM and 10GBM is 1.67×10^{-2} cm^3 g^{-1} and 3.44×10^{-2} cm^3 g^{-1} whereas the pore diameter is 10.07 nm and 10GBM is 11.33 nm, respectively. Such observation suggests that the 10GBM heterostructure is also having higher porosity compared to BM. As a result, 10GBM can act as a superior photocatalyst.

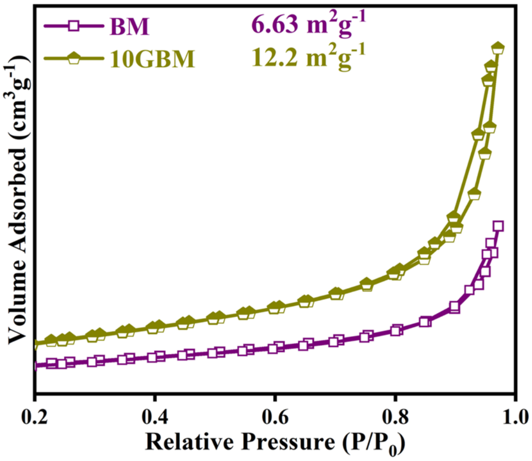

Fig. 8 BET analysis of pristine BM and 10GBM ternary composite.

3.8 Photocatalytic activity

The photocatalytic performance of bare BM, g-C_3N_4, and synthesised composites (5GBM and 10GBM) were examined using visible light (Fig. 9 and S1†). Before irradiating the visible light, the reaction mixture was vigorously stirred in the dark for half an hour to attain the adsorption–desorption equilibrium. The bare BM and g-CN exhibit lower photocatalytic degradation activity in Fig. 9a and b while in the case of ternary nanocomposite (5GBM and 10GBM), upon loading of g-CN on BM photocatalytic activity gradually increases as ~72(3)% and ~82(3)% respectively after 3 h (Fig. 9a, b and d). The

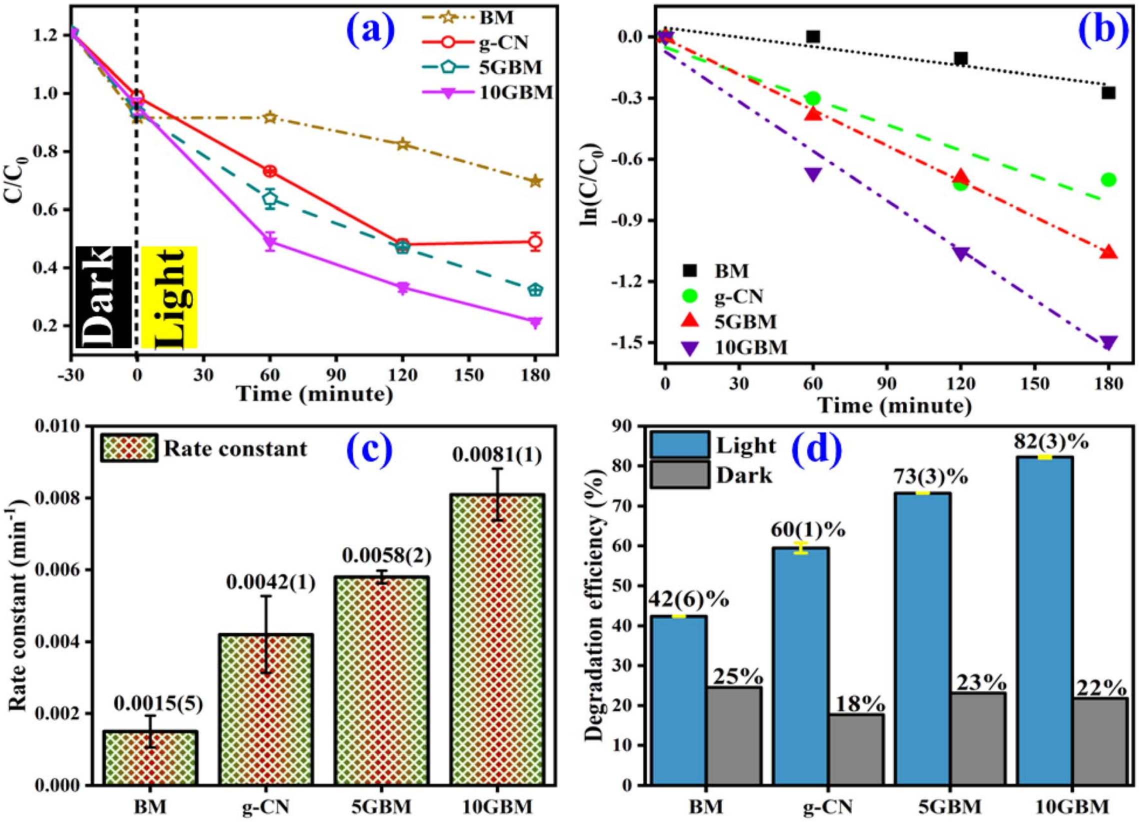

Fig. 9 Photocatalytic deterioration of ofloxacin with time '*t*' (a), displaying pattern with ln C/C_0 at different time period of pristine BM, g-CN and hybrid composites 5GBM and 10GBM (b), rate constant values (c) and bar plot of degradation efficiency in a dark and light environment of all the samples (d).

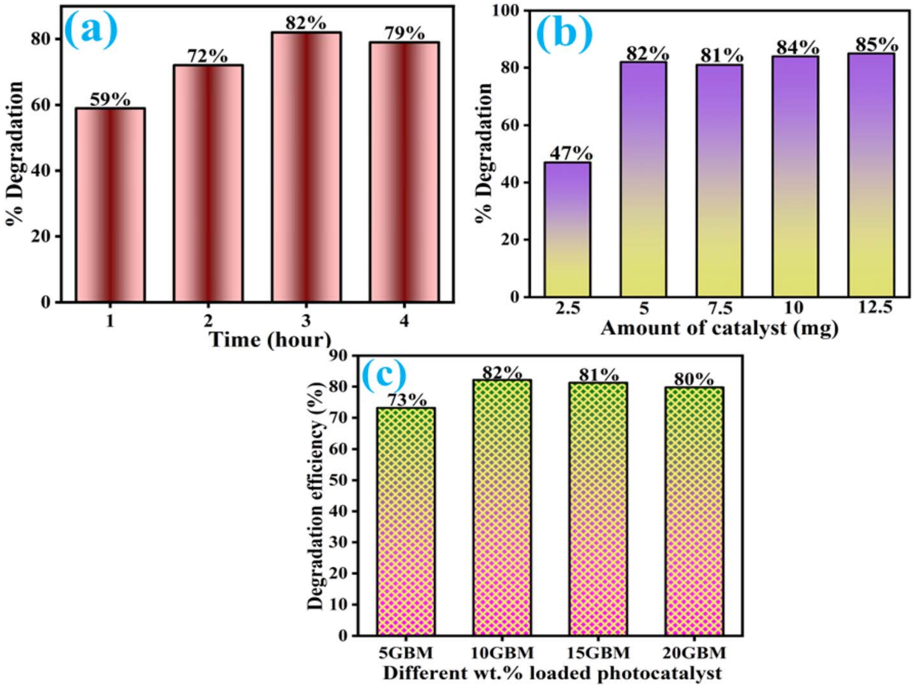

Fig. 10 Optimization of reaction time (a), catalyst dosage (b) and loading of g-CN over BM (c) towards the degradation of ofloxacin.

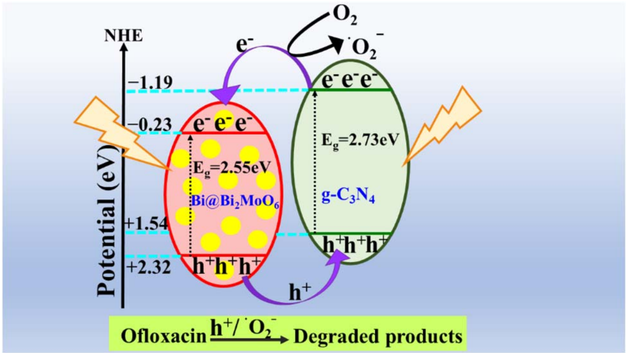

Fig. 11 Representation of the proposed mechanism of type-II heterojunction structure formed by 10GBM photocatalyst.

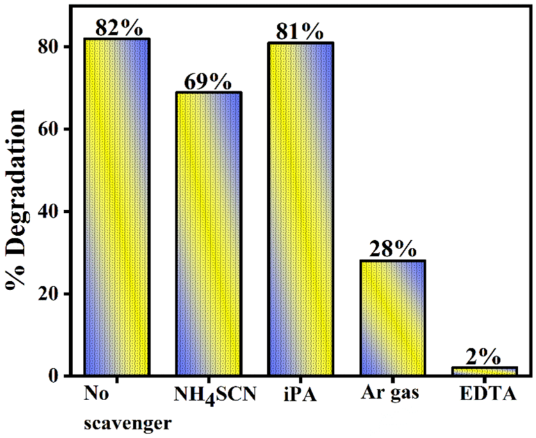

Fig. 12 Effect of Ar purging and NH_4SCN, EDTA, and iPA addition on the photocatalytic activity of the 10GBM catalyst.

photodegradation process followed the pseudo-first-order kinetics as depicted in the following eqn (2) (ref. 21)

$$\ln \frac{C}{C_0} = -kt \tag{2}$$

where C_0 = initial concentration, C = concentration at the time 't' and 'k' = rate constant for pseudo-first-order kinetics.

Substantially, a reaction rate enhances on loading of g-CN and the hybrid nanocomposite 10GBM has the maximum rate constant value 0.0081(1) min^{-1} (Fig. 9c).

To achieve the optimized condition, the effect of reaction time, catalyst amount, and different wt% loading of g-CN was scrutinized (Fig. 10). It was observed in Fig. 10a that on increasing reaction time, the degradation efficiency enhances considerably till 3 h, but after that, no such improvement in the efficiency was observed. It has also been noted (Fig. 10b) that when the catalyst amount increases from 2.5 mg to 5 mg, the degradation efficiency significantly enhances from 47% to 82% due to the greater counts of active sites but with a further increase in the amount, the degradation efficiency remains practically same. Further, evaluated the different wt% loading of g-CN over BM, and it was found that the maximum degradation efficiency was achieved through 10GBM (Fig. 10c), increasing the loading of g-CN above the optimal condition would result in no substantial improvement.

The degree of mineralization was also evaluated along with the degradation studies. Therefore, COD measurements were carried out to study the demineralization of the organic matter[39] using the 10GBM composite. The demineralisation efficiency (DE) was evaluated from the following eqn (3)

$$\text{DE} = \frac{\text{COD}_\text{i} - \text{COD}_\text{f}}{\text{COD}_\text{i}} \times 100 \tag{3}$$

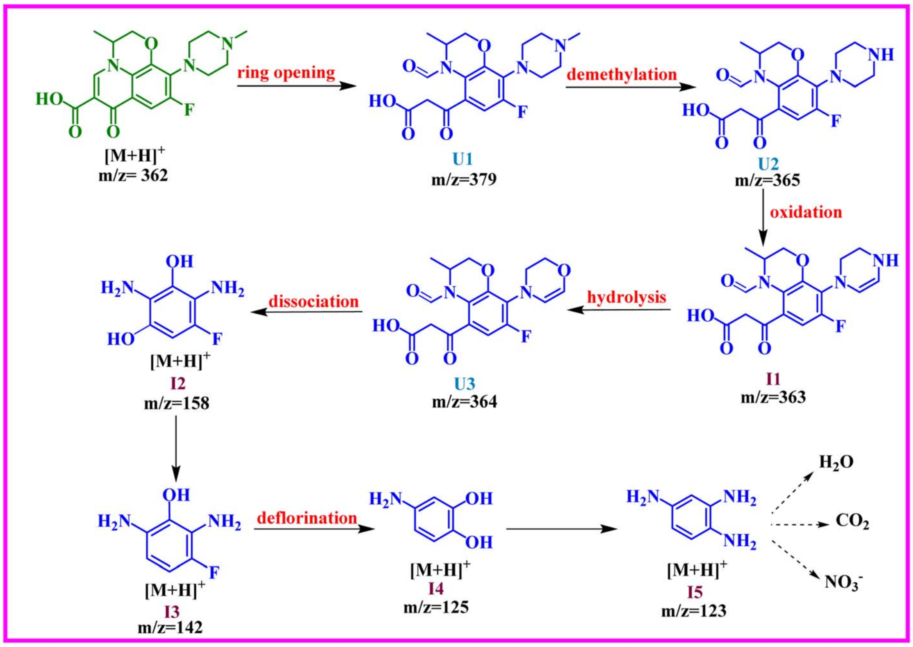

Scheme 1 A plausible mechanism for the degradation of ofloxacin pollutant by 10GBM photocatalyst.

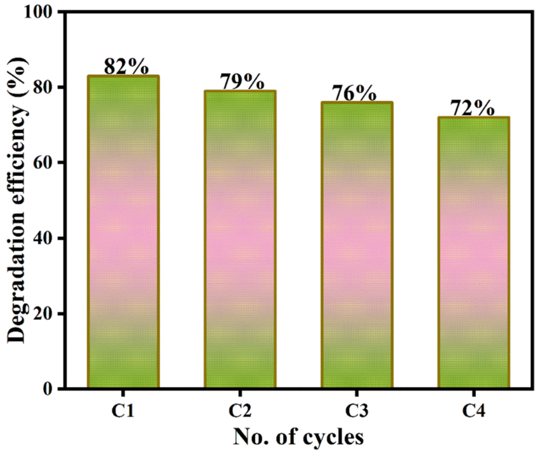

Fig. 13 Reusability using 10GBM composite up to four consecutive cycles of ofloxacin degradation.

The COD of the reaction mixture was decreased from 164 mg L^{-1} to 35.4 mg L^{-1}, which is attributed to ~78.4% demineralization efficiency, which is very close to degradation efficiency, suggesting almost complete degradation of a pollutant without the presence of any residual intermediate.

3.9 Mechanistic study

3.9.1 Proposed mechanism. A heterojunction structure of type II (Fig. 11)[21,40,41] was constructed on the formation of electron–hole pairs produced by excitation *via* a band gap to study the proposed reaction mechanism. The following equation calculates the band energy values of BM and g-CN to validate the mechanism[42]

$$E_{\mathrm{CB}} = E_{\mathrm{VB}} - E_{\mathrm{g}},$$

$$E_{\mathrm{VB}} = X - E_{\mathrm{e}} + 0.5E_{\mathrm{g}}$$

E_{VB} = energy of the valence band, E_{CB} = energy of the conduction band, X= electronegativity of free electron, E_{e} = energy of free electron, E_{g} = band gap energy.

The values of CB and VB of BM and g-CN are −0.23 eV and +2.32 eV (ref. 43) and −1.19 eV and +1.54 eV (ref. 44) respectively. Now, in the 10GBM, the primary reaction occurs in the presence of light irradiation when it falls on the semiconductor. Then the charge carriers (e^{-} and h^{+}) will generate, and electrons (e^{-}) will excite to the CB from the VB and concurrently leave behind the holes (h^{+}) in the VB. Therefore, for the photocatalytic reaction to occur lower redox potential is required so according to the respective (type-II) mechanism, the electrons that are excited to the conduction band of g-CN migrating to the conduction of BM and holes that correspond to the valence band of BM will transfer to the valence band of g-CN, which reduces the recombination of the photogenerated charge carriers (electron–hole pair). Hydroxyl radical production is unfavourable here as the reduction potential is lower than the $^{-}$OH/$^{\bullet}$OH redox couple.[10]

3.9.2 Scavenger studies. Several control studies were investigated to verify the role of reactive entities (Fig. 12). It was observed that upon the addition of NH_4SCN, the degradation efficiency decreased from 82% to 69% and by that of EDTA, it was reduced to 2%, as they function like a hole scavenger so accordingly suppress the oxidation of the pollutant (ofloxacin) with the hole. Additionally, the degradation efficiency was reduced to 28% after Ar gas purging

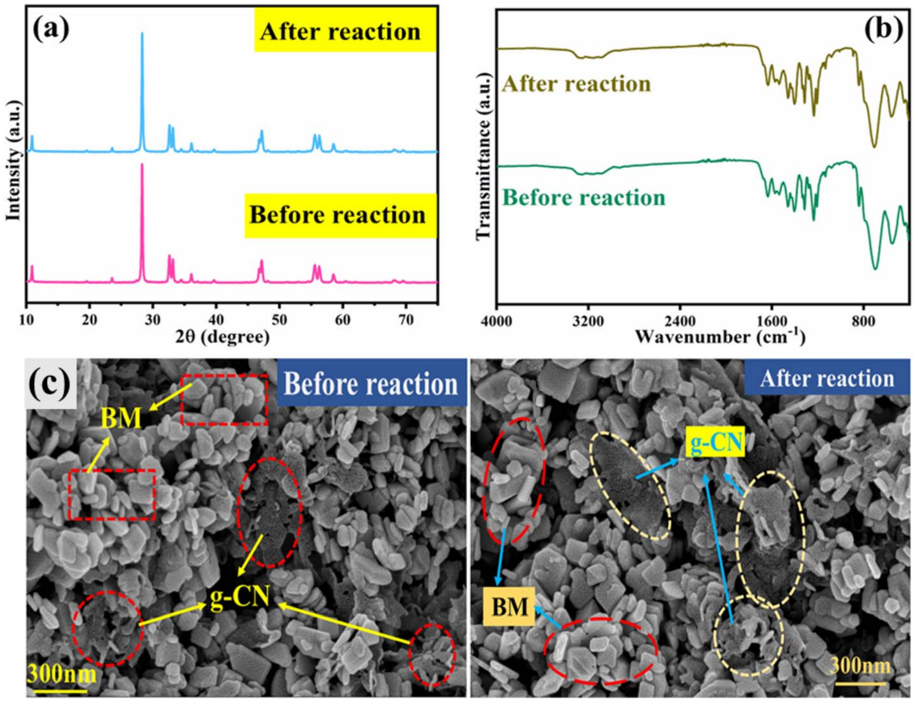

Fig. 14 Before and after reaction XRD and FTIR respectively (a and b) and FESEM (c) of 10GBM photocatalyst.

Table 1 Comparative study of degradation efficiency using different catalysts for ofloxacin

S. no.	Catalyst	Degradation efficiency	Light source	References
1.	$AgBr/WO_3$	82.5%	Solar	47
2.	$BiOCl/TiO_2$	70%	Solar	48
3.	ZnO/CdS	73%	Visible	49
4.	CdS	79%	Visible	50
5.	CdS/TiO_2	86%	Visible	51
6.	Bi-doped $g\text{-}C_3N_4/Bi_2MoO_6$	82%	Visible	This work

resulting in a lowering of the $^{\bullet}O_2^-$ production by eliminating O_2 from a reaction solution. All the conclusions support that the holes (h^+) and superoxide radicals ($^{\bullet}O_2^-$) act as reactive species in the degradation mechanism.[45,46] However, the degradation efficiency does not alter significantly with the presence of isopropyl alcohol (iPA) which shows that hydroxyl radicals ($^{\bullet}OH$) are not participating in the degradation process.

3.9.3 HRMS studies. HRMS analyses were studied to obtain a detailed understanding of the reaction mechanism in Scheme 1 and Fig. S5.† The peak at *m*/*z* 362 is the corresponding peak of the protonated form of ofloxacin. Furthermore, the signals at *m*/*z* 363 (I1), 158 (I2), 142 (I3), 125 (I4) and 123 (I5) indicate the intermediates formed during the degradation process (marked as I, stands for Identified fragments) and *m*/*z* 379 (U1), 365 (U2), 364 (U3) are the Unidentified fragments. It is worth noticeable that with increasing reaction time, the pollutant is degraded a little more into smaller products after half time as showed by the Identified fragments.

3.9.4 Recyclability and stability. For the application of the photocatalysts, their recyclability and stability are essential. The catalyst was extracted from the reaction mixture once it was completed and used in a successive reaction. The degradation efficiency using 10GBM photocatalyst has been found to decrease by just 10% following the fourth cycle when compared to the first (Fig. 13), hence revealing that the composite has great reusability.

The apparent reduction in the photocatalytic activity can be due to the catalyst loss during washing and separation.

Moreover, the stability of the composite in Fig. 14 was evaluated using FESEM, FTIR, and XRD after and before the photocatalytic reaction. Notably, before-after spectra of FTIR and XRD are nearly identical (Fig. 14). Additionally, the morphology of the catalyst before and after the reaction remains similar as depicted by FESEM analysis. These outcomes confirm the excellent stability of the 10GBM composite.

4. Comparison of degradation efficiency

Notably, the 10GBM hybrid catalyst displays either superior or similar photocatalytic performance in the degradation of ofloxacin compared to many reported catalysts as shown in Table 1.

5. Conclusion

To conclude, this report validates the fabrication of ternary Bi(0)-doped $g\text{-}C_3N_4/Bi_2MoO_6$ nanocomposite and evaluates their photodegradation process using the pharmaceutical drug ofloxacin as a pollutant. Substantially, no additional reducing agent is needed to facilitate the formation of photocatalyst as the methanol which serves as a solvent here also plays the role of reducing agent and reduces Bi(III) to zerovalent Bi during the synthesis of Bi_2MoO_6. Bi(0) is dispersed throughout the Bi_2MoO_6 structure because of an *in situ* hydrothermal reaction. The $g\text{-}C_3N_4$ loading simplifies the process of electron transfer in type-II heterojunction structure. In contrast, the metallic Bi increases the visible light response through the LSPR effect, resulting in better photocatalytic activity in degrading ofloxacin under visible light. The reactive species are holes and superoxide radicals as demonstrated by the controlled experiments. The formation of various intermediates was examined by HRMS, which further provided more clarification to the reaction mechanism. Moreover, the recyclability studies confirmed the catalyst has outstanding stability and reusability. As a result, the current work may pave the way for developing plasmonic element-doped materials intended to remove harmful pollutants from wastewater.

Data availability

The supporting data have been uploaded as part of the ESI.†

Author contributions

Priti Rohilla: writing – original draft, visualization, validation, methodology, investigation, formal analysis, data curation, conceptualization. Bonamali Pal: visualization, supervision, resources, project administration, writing – review & editing, funding acquisition. Raj Kumar Das: writing – review & editing, visualization, supervision, project administration, resources, formal analysis, funding acquisition.

Conflicts of interest

The authors declare that they have no known competing financial interests or personal relationships that could have appeared to influence the work reported in this paper.

Acknowledgements

The authors are thankful to SPMS, TIET for their support with XRD and FESEM analysis, and we are grateful to DST-FIST (Grant number: SR/FST/CS-II/2018/69) for providing the HRMS facility at TIET-Patiala and SPRINT Testing Solution in Mumbai for HRTEM, and XPS analysis. The authors are thankful to Dr O. P. Pandey and Mr Abhishek Chandel for the electrochemical measurements, and Dr Soumen Basu and Mr Suvankar Sau for the BET analysis. Moreover, the authors express gratitude to the TIET-VT Centre of Excellence for Emerging Materials (CEEMS) for FTIR measurements. The authors express gratitude to Mr Samarjit Mandal for providing the ICDD data. The authors also acknowledge Mr Bimalpreet Singh and Dr Amit Dhir for the COD measurements.

References

1 S. H. Ammar, F. D. Ali, H. J. Hadi and Z. H. Jabbar, Visible-light-induced photodegradation of ofloxacin antibiotic by facile assembled $BiFeO_3$/Bi-modified g-C_3N_4 heterojunctions, *Mater. Sci. Semicond. Process.*, 2023, **171**, 108026.

2 S. Adhikari and D. H. Kim, Synthesis of Bi_2S_3/Bi_2WO_6 hierarchical microstructures for enhanced visible light driven photocatalytic degradation and photoelectrochemical sensing of ofloxacin, *Chem. Eng. J.*, 2018, **354**, 692–705.

3 T. Chankhanittha and S. Nanan, Visible-light-driven photocatalytic degradation of ofloxacin (OFL) antibiotic and Rhodamine B (RhB) dye by solvothermally grown ZnO/Bi_2MoO_6 heterojunction, *J. Colloid Interface Sci.*, 2021, **582**, 412–427.

4 P. Chen, L. Blaney, G. Cagnetta, J. Huang, B. Wang, Y. Wang, S. Deng and G. Yu, Degradation of Ofloxacin by Perylene Diimide Supramolecular Nanofiber Sunlight-Driven Photocatalysis, *Environ. Sci. Technol.*, 2019, **53**, 1564–1575.

5 Q. Shang, X. Liu, M. Zhang, P. Zhang, Y. Ling, G. Cui, W. Liu, X. Shi, J. Yue and B. Tang, Photocatalytic degradation of ofloxacin antibiotic wastewater using TS-1/C_3N_4 composite photocatalyst: Reaction performance optimisation and estimation of wastewater component synergistic effect by artificial neural network and genetic algorithm, *Chem. Eng. J.*, 2022, **443**, 136354.

6 Q. Su, J. Li, H. Yuan, B. Wang, Y. Wang, Y. Li and Y. Xing, Visible-light-driven photocatalytic degradation of ofloxacin by g-C_3N_4/NH_2-MIL-88B(Fe) heterostructure: Mechanisms, DFT calculation, degradation pathway and toxicity evolution, *Chem. Eng. J.*, 2022, **427**, 131594.

7 W. Chen, Z. Xing, N. Zhang, T. Cheng, B. Ren, X. Liu, Z. Wang, Z. Li and W. Zhou, Hierarchical $Bi_2Fe_4O_9$/BiOI S-scheme heterojunctions with exceptional hydraulic shear induced photo-piezoelectric catalytic activity, *npj Clean Water*, 2024, **7**, 86.

8 H. Li, W. Zhang and Y. Liu, HZSM-5 zeolite supported boron-doped TiO_2 for photocatalytic degradation of ofloxacin, *J. Mater. Res. Technol.*, 2020, **9**, 2557–2567.

9 K. Rabé, L. Liu, N. A. Nahyoon, Y. Zhang, A. M. Idris, J. Sun and L. Yuan, Fabrication of high efficiency visible light Z-scheme heterostructure photocatalyst g-C_3N_4/Fe0(1%)/TiO_2 and degradation of rhodamine B and antibiotics, *J. Taiwan Inst. Chem. Eng.*, 2019, **96**, 463–472.

10 P. Rohilla, B. Pal and R. K. Das, Bi-doped g-C_3N_4/Bi_2WO_6 ternary composites for superior photocatalytic degradation of reactive orange 16 under visible light irradiation, *J. Ind. Eng. Chem.*, 2025, **141**, 456–467.

11 J. Wang, L. Tang, G. Zeng, Y. Liu, Y. Zhou, Y. Deng, J. Wang and B. Peng, Plasmonic Bi metal deposition and g-C_3N_4 coating on Bi_2WO_6 Microspheres for Efficient visible light Photocatalysis, *ACS Sustainable Chem. Eng.*, 2017, **5**, 1062–1072.

12 H. Huang, J. Zhao, H. Guo, B. Weng, H. Zhang, R. A. Saha, M. Zhang, F. Lai, Y. Zhou, R. Z. Juan, P. C. Chen, S. Wang, J. A. Steele, F. Zhong, T. Liu, J. Hofkens, Y. M. Zheng, J. Long and M. B. J. Roeffaers, Noble-Metal-Free High-Entropy Alloy Nanoparticles for Efficient Solar-Driven Photocatalytic CO_2 Reduction, *Adv. Mater.*, 2024, **36**, 2313209.

13 W. Cheng, L. Wang, H. Lao, Y. Wei, J. Xu and B. Weng, Unraveling the Plasmonic Effect of Au in Promoting Photocatalytic H_2 Generation and Organic Synthesis, *ACS Sustainable Chem. Eng.*, 2024, **12**, 17026–17034.

14 H. Zhang, Y. Gao, S. Meng, Z. Wang, P. Wang, Z. Wang, C. Qiu, S. Chen, B. Weng and Y. M. Zheng, Metal Sulfide S-Scheme Homojunction for Photocatalytic Selective Phenylcarbinol Oxidation, *Adv. Sci.*, 2024, **11**, 2400099.

15 Q. Liang, M. Zhang, C. Yao, C. Liu, S. Xu and Z. Li, High performance visible-light driven photocatalysts of Bi_2MoO_6-g-C_3N_4 with controllable solvothermal fabrication, *J. Photochem. Photobiol., A*, 2017, **332**, 357–363.

16 Z. Zhao, W. Zhang, Y. Sun, J. Yu, Y. Zhang, H. Wang, F. Dong and Z. Wu, Bi Cocatalyst/Bi_2MoO_6 Microspheres Nanohybrid with SPR-Promoted Visible-Light Photocatalysis, *J. Phys. Chem. C*, 2016, **120**, 11889–11898.

17 W. Guo, K. Fan, J. Zhang and C. Xu, 2D/2D Z-scheme Bi_2WO_6/Porous-g-C_3N_4 with synergy of adsorption and visible-light-driven photodegradation, *Appl. Surf. Sci.*, 2018, **447**, 125–134.

18 Y. Huang, S. Kang, Y. Yang, H. Qin, Z. Ni, S. Yang and X. Li, Facile synthesis of Bi/Bi_2WO_6 nanocomposite with enhanced photocatalytic activity under visible light, *Appl. Catal., B*, 2016, **196**, 89–99.

19 B. J. Rani, R. Yuvakkumar, G. Ravi, M. Pannipara, A. G. Al-Sehemi and D. Velauthapillai, Bi_2MoO_6 hierarchical microflowers for electrochemical oxygen evolution reaction, *Int. J. Hydrogen Energy*, 2021, **46**, 18719–18728.

20 V. D. Dang, J. Adorna, T. Annadurai, T. A. N. Bui, H. L. Tran, L. Y. Lin and R. A. Doong, Indirect Z-scheme nitrogen-doped carbon dot decorated Bi_2MoO_6/g-C_3N_4 photocatalyst for enhanced visible-light-driven degradation of ciprofloxacin, *Chem. Eng. J.*, 2021, **422**, 130103.

21 P. Rohilla, B. Pal and R. K. Das, Improved photocatalytic degradation of rhodamine B by g-C_3N_4 loaded $BiVO_4$ nanocomposites, *Heliyon*, 2023, **9**, e21900.

22 D. Y. Liu, J. H. Dong, F. M. Liu, X. F. Gao, Y. Yu, S. B. Zhang, L. M. Dong and Y. K. Guo, Synthesis and photocatalytic performance of g-C_3N_4 composites, *J. Ovonic Res.*, 2019, **15**, 239–246.

23 L. Wang, Z. Liu, D. Wang, S. Ni, D. Han, W. Wang and L. Niu, Tailoring hetero structured Bi_2MoO_6/Bi_2S_3 nanobelts for highly selective photoelectrochemical analysis of gallic acid at drug level, *Biosens. Bioelectron.*, 2017, **94**, 107–114.

24 F. Xu, J. Wang, N. Zhang, H. Liang and H. Sun, Simultaneously generating Bi quantum dot and oxygen vacancy on Bi_2MoO_6 nanosheets for boosting photocatalytic selective alcohol oxidation, *Appl. Surf. Sci.*, 2022, **575**, 151738.

25 J. Bai, X. Li, Z. Hao and L. Liu, Enhancement of 3D Bi_2MoO_6 mesoporous spheres photocatalytic performance by vacancy engineering, *J. Colloid Interface Sci.*, 2020, **560**, 510–518.

26 D. S. Vavilapalli, R. G. Peri, R. K. Sharma, U. K. Goutam, B. Muthuraaman, M. S. Ramachandra Rao and S. Singh, g-$C_3N_4/Ca_2Fe_2O_5$ heterostructures for enhanced photocatalytic degradation of organic effluents under sunlight, *Sci. Rep.*, 2021, **11**, 19639.

27 Z. Mao, J. Chen, Y. Yang, L. Bie, B. D. Fahlman and D. Wang, Modification of surface properties and enhancement of photocatalytic performance for g-C_3N_4 via plasma treatment, *Carbon*, 2017, **123**, 651–659.

28 Y. Wang, S. Zhao, Y. Zhang, J. Fang, Y. Zhou, S. Yuan, C. Zhang and W. Chen, One-pot synthesis of K-doped g-C_3N_4 nanosheets with enhanced photocatalytic hydrogen production under visible-light irradiation, *Appl. Surf. Sci.*, 2018, **440**, 258–265.

29 M. Zhu, S. Kim, L. Mao, M. Fujitsuka, J. Zhang, X. Wang and T. Majima, Metal-Free Photocatalyst for H_2 Evolution in Visible to Near-Infrared Region: Black Phosphorus/Graphitic Carbon Nitride, *J. Am. Chem. Soc.*, 2017, **139**, 13234–13242.

30 N. Li, L. Zhu, W. De Zhang, Y. X. Yu, W. H. Zhang and M. F. Hou, Modification of TiO_2 nanorods by Bi_2MoO_6 nanoparticles for high performance visible-light photocatalysis, *J. Alloys Compd.*, 2011, **509**, 9770–9775.

31 M. Sierra, E. Borges, P. Esparza, J. Méndez-Ramos, J. Martín-Gil and P. Martín-Ramos, Photocatalytic activities of coke carbon/g-C_3N_4 and Bi metal/Bi mixed oxides/g-C_3N_4 nanohybrids for the degradation of pollutants in wastewater, *Sci. Technol. Adv. Mater.*, 2016, **17**, 659–668.

32 E. Vesali-Kermani, A. Habibi-Yangjeh, H. Diarmand-Khalilabad and S. Ghosh, Nitrogen photo fixation ability of g-C_3N_4 nanosheets/Bi_2MoO_6 heterojunction photocatalyst under visible-light illumination, *J. Colloid Interface Sci.*, 2020, **563**, 81–91.

33 W. Xue, D. Huang, J. Li, G. Zeng, R. Deng, Y. Yang, S. Chen, Z. Li, X. Gong and B. Li, Assembly of AgI nanoparticles and ultrathin g-C_3N_4 nanosheets codecorated Bi_2WO_6 direct dual Z-scheme photocatalyst: An efficient, sustainable and heterogeneous catalyst with enhanced photocatalytic performance, *Chem. Eng. J.*, 2019, **373**, 1144–1157.

34 T. Wang, Y. Bai, W. Si, W. Mao, Y. Gao and S. Liu, Heterogeneous photo-Fenton system of novel ternary $Bi_2WO_6/BiFeO_3$/g-C_3N_4 heterojunctions for highly efficient degrading persistent organic pollutants in wastewater, *J. Photochem. Photobiol., A*, 2021, **404**, 112856.

35 Y. Su, G. Tan, T. Liu, L. Lv, Y. Wang, X. Zhang, Z. Yue, H. Ren and A. Xia, Photocatalytic properties of $Bi_2WO_6/BiPO_4$ Z-scheme photocatalysts induced by double internal electric fields, *Appl. Surf. Sci.*, 2018, **457**, 104–114.

36 D. Chen, Q. Hao, Z. Wang, H. Ding and Y. Zhu, Influence of phase structure and morphology on the photocatalytic activity of bismuth molybdates, *CrystEngComm*, 2016, **18**, 1976–1986.

37 G. Yang, Y. A. Zhu, Y. Liang, J. Yang, K. Wang, Z. Zeng, R. Xu and X. Xie, Crystal defect-mediated {0 1 0} facets of Bi_2MoO_6 nanosheets for removal of TC: Enhanced mechanism and degradation pathway, *Appl. Surf. Sci.*, 2021, **539**, 148038.

38 A. Kundu, S. Sharma and S. Basu, Modulated BiOCl nanoplates with porous g-C_3N_4 nanosheets for photocatalytic degradation of color/colorless pollutants in natural sunlight, *J. Phys. Chem. Solids*, 2021, **154**, 110064.

39 S. Singla, P. Devi and S. Basu, Revolutionizing the Role of Solar Light Responsive $BiVO_4$/BiOBr Heterojunction Photocatalyst for the Photocatalytic Deterioration of Tetracycline and Photo electro catalytic Water Splitting, *Materials*, 2023, **16**, 5661.

40 C. Murugan, M. Karnan, M. Sathish and A. Pandikumar, Construction of heterostructure based on hierarchical Bi_2MoO_6 and g-C_3N_4 with ease for impressive performance in photoelectrocatalytic water splitting and supercapacitor, *Catal. Sci. Technol.*, 2020, **10**, 2427–2442.

41 K. Wu, X. Qiu, Y. Luo and C. Zhang, Oxygen Vacancy Mediated-Bismuth Molybdate/Graphitic Carbon Nitride Type II Heterojunction Chemiresistor for Efficient NH_3 Detection at Room Temperature, *ACS Sens.*, 2024, **9**, 6698–6708.

42 N. Tian, H. Huang, Y. He, Y. Guo, T. Zhang and Y. Zhang, Mediator-free direct Z-scheme photocatalytic system: $BiVO_4$/g-C_3N_4 organic–inorganic hybrid photocatalyst with highly efficient visible-light-induced photocatalytic activity, *Dalton Trans.*, 2015, **44**, 4297–4307.

43 T. Han, Y. Chen and H. Shi, Construction of a Bi_2MoO_6/CoO_x/Au system with a dual-channel charge transfer path for enhanced tetracycline degradation, *Catal. Sci. Technol.*, 2022, **12**, 5565–5574.

44 W. Hu, J. Yu, X. Jiang, X. Liu, R. Jin, Y. Lu, L. Zhao, Y. Wu and Y. He, Enhanced photocatalytic activity of g-C_3N_4 via modification of $NiMoO_4$ nanorods, *Colloids Surf., A*, 2017, **514**, 98–106.

45 B. R. Shah and U. D. Patel, Mechanistic aspects of photocatalytic degradation of lindane by TiO_2 in the presence of oxalic acid and EDTA as hole-scavengers, *J. Environ. Chem. Eng.*, 2021, **9**, 105458.

46 M. Chahkandi and M. Zargazi, New water based EPD thin $BiVO_4$ film: Effective photocatalytic degradation of Amoxicillin antibiotic, *J. Hazard. Mater.*, 2020, **389**, 121850.

47 J. Piriyanon, P. Takhai, S. Patta, T. Chankhanittha, T. Senasu, S. Nijpanich, S. Juabrum, N. Chanlek and S. Nanan, Performance of sunlight responsive WO_3/AgBr

heterojunction photocatalyst toward degradation of Rhodamine B dye and ofloxacin antibiotic, *Opt. Mater.*, 2021, **121**, 111573.

48 Q. Wang, P. Li, Z. Zhang, C. Jiang, K. Zuojiao, J. Liu and Y. Wang, Kinetics and mechanism insights into the photodegradation of tetracycline hydrochloride and ofloxacin mixed antibiotics with the flower-like BiOCl/TiO_2 heterojunction, *J. Photochem. Photobiol., A*, 2019, **378**, 114–124.

49 T. Senasu, T. Chankhanittha, K. Hemavibool and S. Nanan, Visible-light-responsive photocatalyst based on ZnO/CdS nanocomposite for photodegradation of reactive red azo dye and ofloxacin antibiotic, *Mater. Sci. Semicond. Process.*, 2021, **123**, 105558.

50 M. Kaur, S. K. Mehta and S. K. Kansal, Visible light driven photocatalytic degradation of ofloxacin and malachite green dye using cadmium sulphide nanoparticles, *J. Environ. Chem. Eng.*, 2018, **6**, 3631–3639.

51 A. Kaur, A. Umar, W. A. Anderson and S. K. Kansal, Facile synthesis of CdS/TiO_2 nanocomposite and their catalytic activity for ofloxacin degradation under visible illumination, *J. Photochem. Photobiol., A*, 2018, **360**, 34–43.